

Experimental and Numerical Assessment of MRI-Induced Temperature Change and SAR Distributions in Phantoms and In Vivo

Sukhoon Oh,¹ Andrew G. Webb,^{2,3} Thomas Neuberger,² BuSik Park,^{1,4} and Christopher M. Collins^{1,4*}

It is important to accurately characterize the heating of tissues due to the radiofrequency energy applied during MRI. This has led to an increase in the use of numerical methods to predict specific energy absorption rate distributions for safety assurance in MRI. To ensure these methods are accurate for actual MRI coils, however, it is necessary to compare to experimental results. Here, we report results of some recent efforts to experimentally map temperature change and specific energy absorption rate in a phantom and in vivo where the only source of heat is the radiofrequency fields produced by the imaging coil. Results in a phantom match numerical simulation well, and preliminary results in vivo show measurable temperature increase. With further development, similar methods may be useful for verifying numerical methods for predicting specific energy absorption rate distributions and in some cases for directly measuring temperature changes and specific energy absorption rate induced by the radiofrequency fields in MRI experiments. Magn Reson Med 63:218–223, 2010. © 2009 Wiley-Liss, Inc.

Key words: specific absorption rate; MR thermography; simulation; proton resonance frequency; MRI

Specific energy absorption rate (SAR) is the power absorbed in tissue due to conduction currents induced by alternating electromagnetic fields, and is the quantity regulated most often in a number of industries to ensure safe levels of heating in tissues exposed to RF or microwave-frequency electromagnetic fields. Although temperature increase is more directly related to potential hazard, SAR rather than temperature is often used due to challenges in measuring or predicting temperature increases in vivo. Current widely accepted guidelines in MRI provide regulations for the core body temperature and temperature in various locations in the body, but also for the whole-body average SAR, head-average SAR, partial-body SAR, and the maximum SAR in any 10 g of tissue (the maximum local SAR) (1). While the whole-body average SAR, head-average SAR, and partial-body SAR can be determined by

estimates of the total amount of RF power dissipated in the subject and the mass of the subject and/or portion of the subject exposed to RF fields, determination of the maximum local SAR requires more sophisticated methods.

Recent years have seen a dramatic increase in the use of numerical calculations considering heterogeneous human anatomies to predict SAR distributions during MRI (2). With the emergence of transmit array technologies, where it is possible to have a very wide range of maximum local SAR for a given patient, array configuration, and average SAR (3), it seems likely that methods to rapidly and accurately predict SAR distributions will become more critical (4,5). While numerical calculations have shown agreement with experiment in amplitude of RF field (B_1) distributions and signal intensity distributions, this does not allow a general assumption that there would also be such good agreement between calculated and experimental SAR distributions. The SAR distribution depends on the available current paths via the distribution of electrical conductivity throughout the subject, and thus varies greatly from person to person much more so than does the B_1 field (6). For example, at low frequencies where the sample has little effect on the B_1 field distribution, two samples with very different geometries and necessarily very different SAR distributions can have nearly identical B_1 field distributions when imaged with the same coil.

Temperature changes can be mapped through changes in the MR signal with a variety of methods (7). Some previous works have measured temperature changes with MR due to heating by RF coils (8–10) and at least one has estimated SAR from the MR signal due to heating with a microwave diathermy array (11). Here, we present MR-based measurements of the SAR distribution based on temperature increase and compare to numerical calculations for a homogeneous phantom within a transmit/receive quadrature head coil. We then perform a separate experiment to examine the feasibility of directly measuring the SAR produced by proton decoupling sequences in vivo.

MATERIALS AND METHODS

Phantom Experiments at 3 T

The first series of experiments was performed with a phantom on a 3 T whole-body imaging system (Bruker Corporation, Billerica, MA). A phantom was placed in the center of a transmit/receive head-sized quadrature birdcage coil, used both for RF-induced heating and the MR imaging used to monitor temperature changes. The dimensions of the phantom and coil are given in Fig. 1. The phantom was

¹Department of Radiology, The Pennsylvania State University College of Medicine, Hershey, Pennsylvania, USA

²Department of Bioengineering, The Pennsylvania State University, University Park, Pennsylvania, USA

³Department of Radiology, Leiden University Medical Center, Leiden, The Netherlands

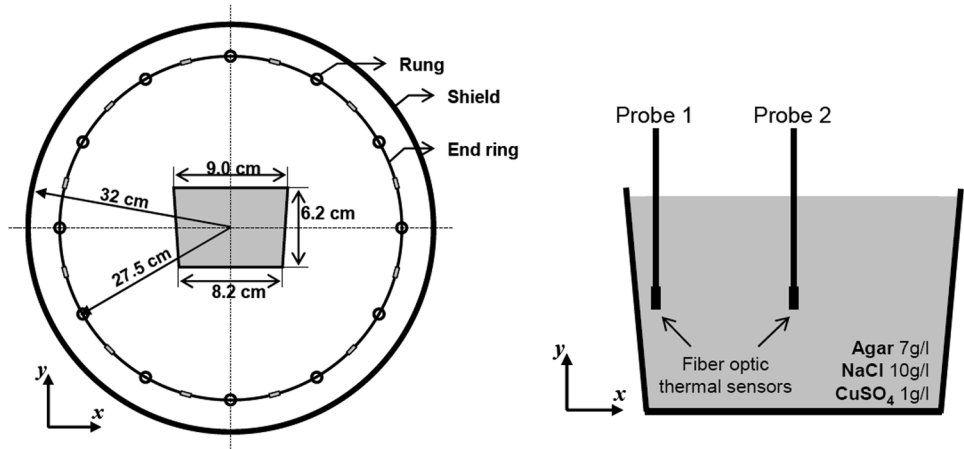
⁴Department of Bioengineering, The Pennsylvania State University College of Medicine, Hershey, Pennsylvania, USA

*Correspondence to: Christopher M. Collins, PhD, NMR/MRI Building, H066, 500 University Drive, Hershey, PA 17033. E-mail: cmcollins@psu.edu

Received 22 December 2008; revised 14 July 2009; accepted 17 July 2009. DOI 10.1002/mrm.22174

Published online 25 September 2009 in Wiley InterScience (www.interscience.wiley.com).

FIG. 1. Coil and sample geometry. Left: sample (gray) was placed at the center of a quadrature 12-element birdcage coil. Length of shield, coil, and sample is 33 cm, 29 cm, and 15 cm, respectively. Right: For preliminary experiments, thermo-optic probes were placed near the surface and at the center of the phantom on the central axial plane.



created by dissolving agar (7 g/L), NaCl (10 g/L), and CuSO_4 (1 g/L) in hot water and then allowing the solution to cool and solidify in a plastic former. The volume of the agar-gel phantom was 0.8 L and its weight was 843 g. The density of the conductive agar-gel was 1054 kg/m^3 .

Preliminary Experiment to Verify Linearity of Temperature Change With Time

The heat equation for a nonperfused material with an internal heat source (in our case, SAR) can be written as

$$\rho c \frac{dT}{dt} = \nabla \cdot (k \nabla T) + \text{SAR} \rho \quad [1]$$

where ρ is material density, c is heat capacity, T is temperature, k is thermal conductivity, and t is time. Immediately before the application of electromagnetic energy (i.e., when $\text{SAR} = 0$), if the material is at thermal equilibrium, then $\nabla \cdot (k \nabla T) = 0$. Because thermal conduction requires time and a temperature gradient to affect the temperature distribution, for a short period after initiation of heating, effects of thermal conduction will be negligible and the increase in temperature over time will be directly proportional to the applied SAR. If the applied SAR is constant over time, the temperature increase with time will also be linear during this period. To ensure that our experiments were performed during a period of linear temperature increase and negligible thermal conduction, we performed a preliminary experiment where we measured the temperature increase in the phantom with thermo-optic probes (AccuSens; OpSens, Quebec, Canada) placed at locations of anticipated high SAR (near the surface of the phantom on the central axial plane) and of anticipated low SAR (near the middle of the phantom) as shown in Fig. 1. The phantom was inserted into the RF coil and placed in the bore overnight to achieve thermal equilibrium. Then a multiecho sequence with short pulse repetition time and high RF power was applied to the sample for 40 min.

The power dissipated in the sample was estimated by first connecting high-power attenuators and a digital oscilloscope (TDS 3054C; Tektronix, Beaverton, OR) at the location of the quadrature splitter/combiner in the RF transmit chain and performing digital integration of the RF

pulses applied, and then using a network/spectrum analyzer (HP 4195A; Hewlett Packard, Palo Alto, CA) to estimate losses due to the quadrature splitter/combiner and additional cables to each channel of the coil, as well as quality factors of the two channels of the coil when loaded (Q_l) and unloaded (Q_u). Considering the duty cycle of the pulse sequence and estimating the fraction of the power delivered to the coil that was actually dissipated in the sample as $(1 - Q_l/Q_u)$, we determined that an average of approximately 5.25 W was dissipated in the sample.

The temperatures at the locations of the probes were recorded during heating and for another 2 h after termination of heating.

SAR Mapping

To map the SAR distribution, we first used the proton resonance frequency shift method of MR thermography (7). In the proton resonance frequency method, phase maps are acquired before and after a period of sample heating. The temperature change (ΔT) can then be calculated from the phase change ($\Delta \phi$) as

$$\Delta T = \frac{\Delta \phi}{\alpha \times \gamma \times B_0 \times TE} \quad [2]$$

where α is the temperature-dependent chemical shift coefficient (-0.01 ppm/K for water), γ is the gyromagnetic ratio of hydrogen, B_0 is the strength of the main magnetic field (3 T in our case), and TE is the echo time. The phantom was once again inserted into the birdcage coil and placed inside of the bore overnight to achieve thermal equilibrium before beginning the experiment. The first phase map was acquired with a gradient-echo pulse sequence (echo time/repetition time = 20 ms/100 ms, matrix size = 64×64 , field of view = $120 \times 120 \text{ mm}^2$, 10-mm slice thickness, four averages). Data were acquired from two slices, at the central axial slice ($z = 0 \text{ mm}$) and an off-center slice ($z = 30 \text{ mm}$). The total scan time for the first phase map was 25.6 sec. Then the phantom was heated for 2 min using a spin-echo pulse sequence having high RF power and short pulse repetition time, as in the preliminary experiment, resulting in approximately 5.25

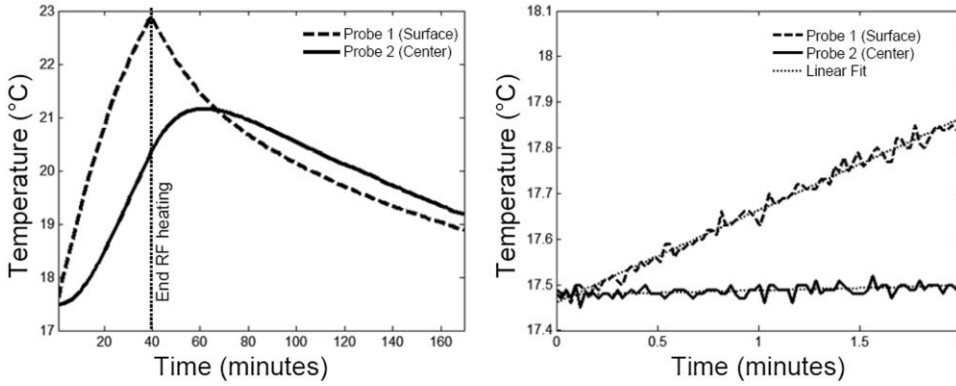


FIG. 2. Temperature at the location of the thermo-optic probes over the duration of the entire preliminary experiment (left) and during the first 2 min of heating (right).

W dissipated in the sample. The second phase map was acquired with the same parameters as the first, but with no averages. The scan time for the second phase map was 6.4 sec. The phase difference ($\Delta\phi$ in Eq. 1) was calculated as the difference between the first and second phase maps.

Using the results of the preliminary experiment, we limited the duration of the SAR mapping experiment to 2 min, a period over which temperature increase was very linear with time. As discussed above, there was negligible contribution from thermal conduction (the first term on the right-hand side of Eq. 1) during this period, so that SAR could be estimated from the change in temperature as

$$\text{SAR} = c_{\text{phantom}} \frac{\Delta T}{\Delta t} \quad [3]$$

where c_{phantom} is the heat capacity of the phantom (approximately 4200 J/kg/°C (12) and Δt is the period of heating, or 120 sec.

Numerical Simulations of Phantom Experiments

Numerical models matching the geometries of the phantom and birdcage coil were created for use with the finite difference time domain method for electromagnetic field calculation. The coil was driven in ideal mode 1 resonance, with appropriate current sources at the locations of the physical capacitors. This method has previously shown very good predictions of experimental B_1 field distributions (13). The conductivity (σ) and the relative permittivity (ϵ_r) of the phantom were set to 1.886 S/m and 77.52, respectively. These values were determined by direct measurement in the gel using an Agilent 85070D Dielectric Probe Kit Agilent Technologies, Santa Clara, CA connected to an Agilent E4991A RF Impedance/Material Analyzer (calibration performed with short-circuit terminator, air, and distilled/deionized water). The cell size in simulation was $2 \times 2 \times 2 \text{ mm}^3$. SAR maps were calculated at the frequency of 125.44 MHz, corresponding to the Larmor frequency of our 3 T system, using commercial software for electromagnetic field calculations (XFDTD; Remcom, State College, PA). After the calculation, the results were scaled so that the power dissipated in the phantom was 5.25 W, as in the experiment. Because the experiment was designed to have minimal effect from thermal conduction, numerical prediction of temperature

increase can also be made by solving Eq. 3 for ΔT using the numerically calculated SAR distribution and values for c_{phantom} and Δt used in experiment.

In Vivo Experiments at 7 T

The in vivo experiments were performed on a horizontal-bore 7-T animal scanner (Varian Inc., Palo Alto, CA) using a 7-cm inner-diameter quadrature birdcage coil. Rats (Sprague-Dawley; ~300 g) were anesthetized using a mixture of isoflurane and oxygen. Body temperature and electrocardiogram signals were monitored continuously throughout the experiment (SA Instruments, Stony Brook, NY). As in the phantom experiments, difference in phase on gradient echo images before and after a heating period was used to determine the temperature change. The in vivo experiments, however, utilized a proton decoupling pulse sequence for heating, utilizing many repetitions of a shorter heating/measurement cycle in series. In order to simulate realistic data acquisition parameters for in vivo ^{13}C spectroscopy, a WALTZ-4 decoupling module was applied for 320 ms, with a 680-ms delay. This was repeated four times, for a total heating period of 4 sec before the each gradient-echo imaging sequence was applied for temperature mapping (matrix 128×128 , pulse repetition time/echo time 50/20 ms, single slice thickness 2 mm). The decoupling (B_2) field used in the decoupling pulse was 625 Hz. The entire decoupling/temperature measurement sequence was repeated 20 times over a period of 120 sec, not including the time required for the initial reference gradient echo scan. Using methods similar to those described for determining power dissipation in the phantom, we estimate 11.0 W were dissipated in the rat during the experiment.

As with the phantom, for a short time after the initiation of heating the change in temperature is proportional to SAR, but more factors (especially the rate of perfusion) can potentially influence the duration of the period of linear increase (14). For this study, a simple linear fit to the temperature data at each location was used to determine the SAR as according to Eq. 3.

RESULTS

The results of the thermo-optic probe measurements of temperature over time at locations near the center and surface of the phantom while heating with a high-SAR

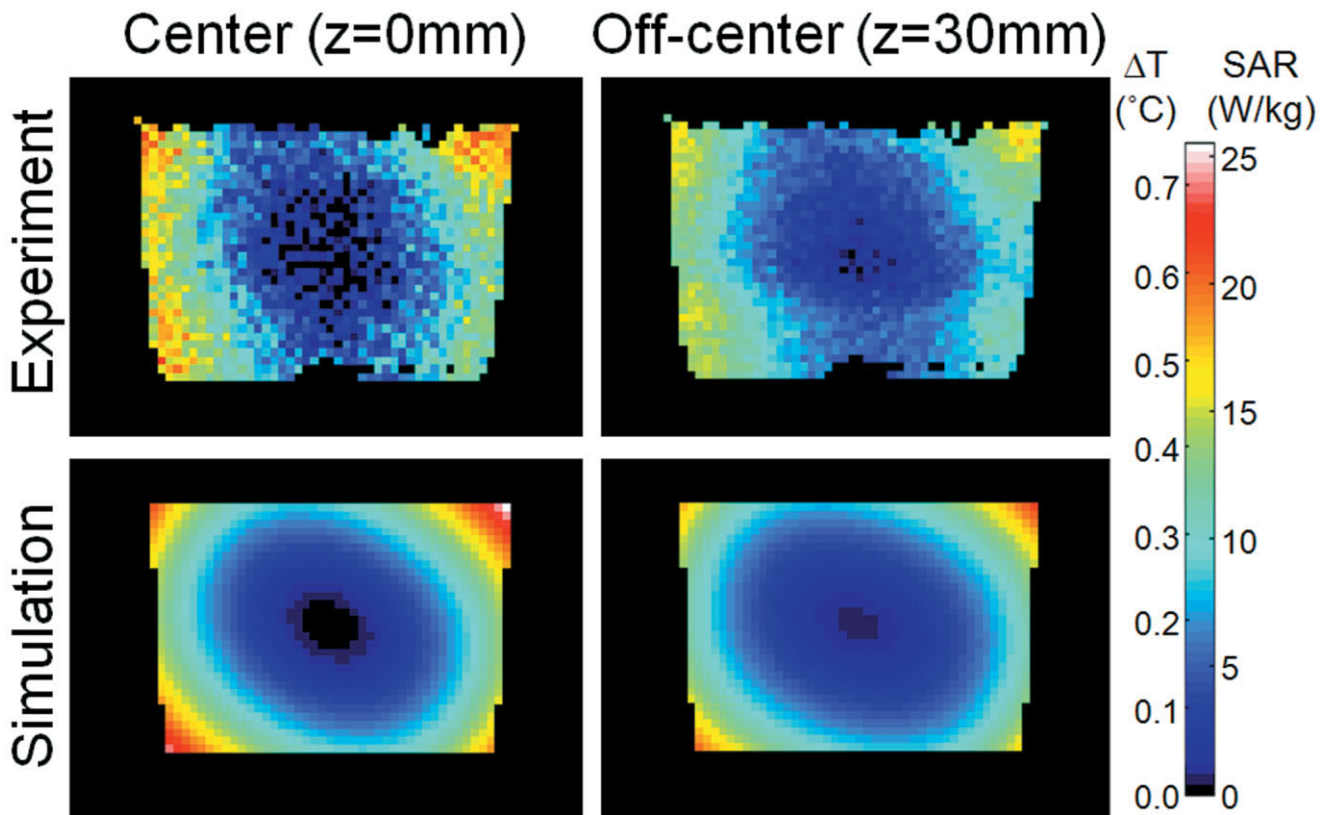


FIG. 3. Temperature increase ($^{\circ}\text{C}$) and SAR (W/kg) in the experiment (top) and corresponding SAR from the simulations (bottom) from axial planes through the central (left) and 30 mm off-center (right) axial planes through phantom.

sequence in the birdcage coil are shown in Fig. 2. After only the first few minutes the temperature change becomes nonlinear with time and the temperature at the center of the phantom (where SAR is expected to be minimal) begins to increase notably, both indications that the contributions of heat conduction are becoming significant. This result prompted us to limit the period of heating to 2 min or less in experiments. Linear fits to the first 2 min of data had χ^2 values less than 0.001, indicating very linear temperature increase with time. Another indication that SAR is the dominant factor at the surface of the phantom and thermal conduction is dominant at the center is seen in the fact that after termination of the RF heating, the temperature at the surface begins to decrease immediately, but that at the center continues to increase for some time before reaching a plateau, followed by a more gradual decrease.

Temperature and corresponding SAR maps from the proton resonance frequency shift MRI are shown in Fig. 3, together with numerically calculated SAR and temperature maps for the same sample and coil. SAR and temperature distributions are related through Eq. 3 in both experiment and simulation. Because these SAR values are for a single voxel (having a mass of about 37.1 mg in the experiment), these numbers cannot be compared directly to local SAR limits, which are now typically written for maximum SAR in any 10-g region (1). In the experiments, the maximum temperature change was 0.63°C at the upper-right corner of the center

slice, where the SAR was $21.5 \text{ W}/\text{kg}$ based on Eq. 3. The averaged SAR on the central axial plane was $8.01 \text{ W}/\text{kg}$ in the experiment. The SAR and temperature distributions from numerical simulations match the experimentally acquired SAR maps well. As expected for a homogeneous phantom in the absence of significant wavelength effects, SAR increases roughly with the square of the radial distance from the middle of the phantom on the planes shown, and the SAR values at the middle of the center-axial slice are lower than those at the center of the off-center slice.

Figure 4 shows results from the in vivo experiments. A gradient echo image of the plane of interest is shown in Fig. 4a. The axial plane passes through the hind legs and abdomen of the animal. The red dot shows the location from which the data for the temperature versus time plot (Fig. 4c) are taken. As shown in Fig. 4b, the regions of tissue showing the highest temperature increase are near the outer surface of the animal, where the electric field produced by the coil is expected to be the largest. Fig. 4c shows a plot of temperature versus time at the location of the red dot in Fig. 4a. A linear fit, from which the SAR at that location is calculated, is also shown. The plot shows a straight line with an r value of 0.91, and there is no evidence of nonlinearity in the plot over the short experimental time and the relatively small temperature increases measured. Finally, Fig. 4d shows a plot of the SAR for each voxel within the imaged slice.

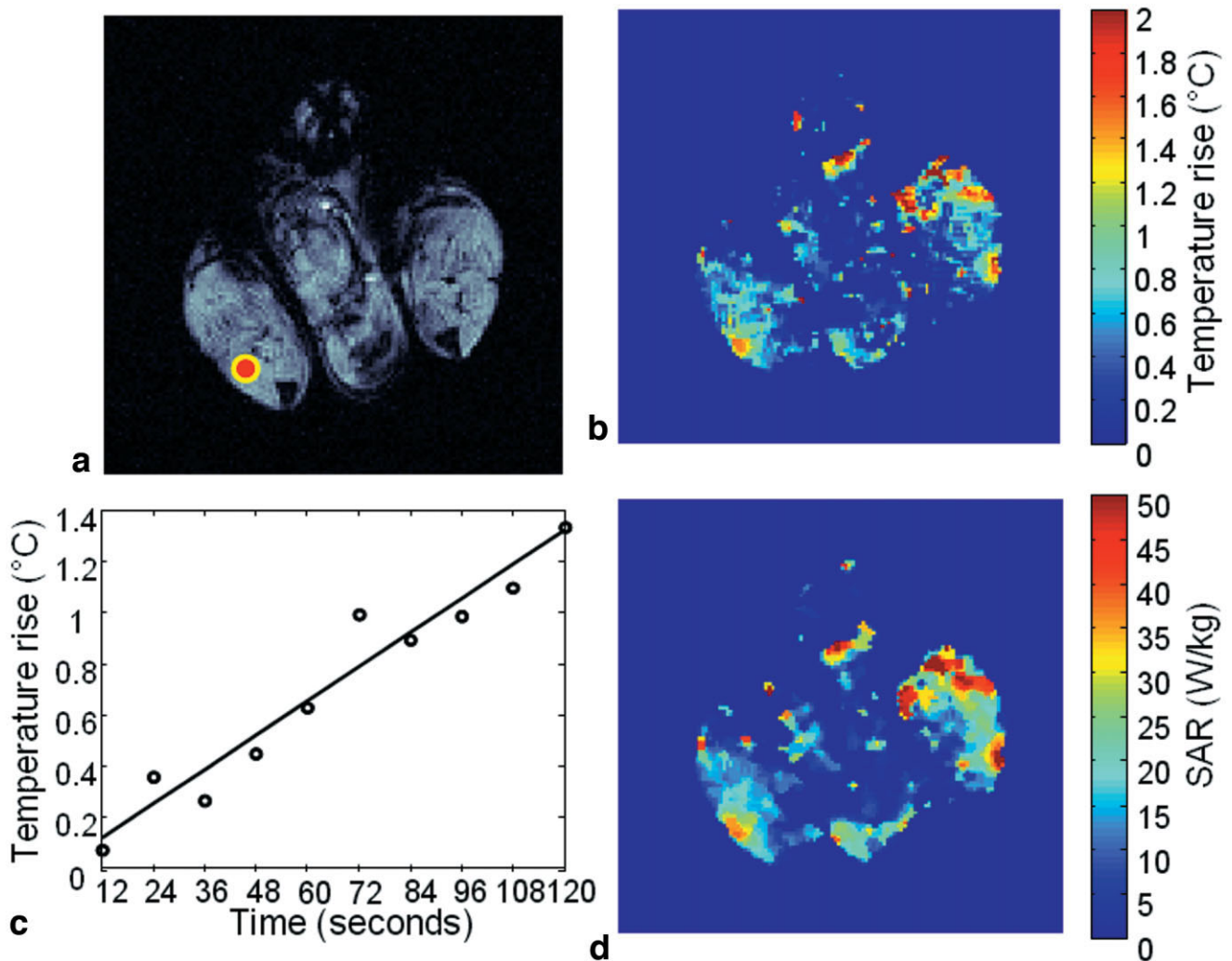


FIG. 4. Results from the in vivo experiments. **a**: Gradient echo image of the plane of interest, with red dot showing the location of data for the temperature time course (**c**). **b**: Temperature increase after 2 min calculated from the phase change between the last gradient echo image and an initial reference scan. **c**: Line plot of temperature versus time at the location of the red dot in (**a**) (every second value is plotted for clarity). A linear fit, from which the SAR at that location is calculated, is also shown. **d**: SAR distribution throughout the slice.

DISCUSSION

One major purpose of this study was to develop and demonstrate a method for examining the accuracy of a numerical method for predicting SAR distributions with comparison to experimental measurement. To accomplish this we first designed an experiment in a phantom with a brief period of heating so that the effects of thermal conduction and perfusion were negligible, meaning that SAR and temperature increase are directly proportional. Temperature increase in phantoms due to RF fields applied through MRI coils has been measured with MR thermography previously (8-10). In one of these prior cases, the distribution of temperature increase was compared to an analytically determined SAR distribution for a sphere in a homogeneous linear RF magnetic field (9). The two distributions were similar when a phantom with very high salinity (680 mM) and conductivity (6.3 S/m) was used, but not in phantoms at lower salinity. In neither of these previous works were the effects of thermal conduction given serious

consideration, and in both works the period of heating (5 to 10 min) was significantly longer than that used here (2 min). In the work presented here, the agreement between the calculated and measured SAR and temperature distributions in Fig. 3 indicate that such measurement of SAR distributions could be valuable in validating numerical methods.

The well-documented differences in SAR distributions within homogeneous phantoms and heterogeneous human anatomies (15) dictate the necessity of exploring the feasibility of such a method in vivo. In Fig. 4, results of an early attempt at measuring MRI-induced heating and SAR distributions in a live rat are shown. While this study was limited in that no calculations matching the experimental setup are yet available, it does show linear temperature increase in much of the animal during the short heating period, indicating that the very simple conversion from temperature to SAR should be valid. In any in vivo measurements of temperature, a potential mitigating factor is

that of temperature-dependent increases in blood flow and perfusion rate. These can cause small phase changes via, for example, inflow effects and altered deoxy/oxyhemoglobin ratios. However, they are highly complex, depending upon the geometry of the vessels and capillaries and, based on results in functional MRI, are likely to be quite small. In the particular case presented here, perfusion changes in muscle are expected to be relatively small (16).

Using a very different approach, the SAR distribution has also been estimated from experimental maps of the magnitude of the circularly polarized component of the B_1 field that induces nuclear precession (17). While this method may have an advantage over that used here in that it does not require a temperature change be induced, it also has significant challenges: either it must be assumed that the RF magnetic field has perfect circular polarization (i.e., there is no counter-rotating or longitudinal component of the B_1 field) or else additional experimental or numerical methods must be applied to estimate the other components.

Whichever experimental methods are used to estimate SAR and/or temperature distributions, they typically require significant time. Thus, numerical predictions of SAR and temperature increase are likely to have continued value in implementing safety limits. Here we have demonstrated a simple method to validate the accuracy of numerical predictions of SAR and temperature in a phantom and demonstrated the feasibility of using such a method in vivo.

ACKNOWLEDGMENTS

Funding: NIH R01 EB000454, NIH R01 EB000895.

REFERENCES

1. International Electrotechnical Commission. International standard, medical equipment—part 2: particular requirements for the safety of magnetic resonance equipment for medical diagnosis, 2nd revision. Geneva: International Electrotechnical Commission; 2002. 88p.
2. Collins CM. Numerical field calculations considering the human subject for engineering and safety assurance in MRI. *NMR Biomed*, in press.
3. Collins CM, Wang Z, Smith MB. A conservative method for ensuring safety within transmit arrays. In: 15th Scientific Meeting and Exhibition of the International Society for Magnetic Resonance in Medicine, Berlin, 2007. p 1092.
4. Mao W, Wang Z, Smith MB, Collins CM. Calculation of SAR for transmit coil arrays. *Concepts Magn Reson* 2007;31B:127–131.
5. Graesslin I, Glaesel D, Biederer S, Vernickel P, Katscher U, Schweser F, Annighoefer B, Dingemans H, Mens G, Yperen GV, Harvey P. Comprehensive RF safety concept for parallel transmission systems. In: 16th ISMRM, Toronto, 2008. p 74.
6. Liu W, Collins CM, Smith MB. Calculations of B_1 distribution, specific energy absorption rate, and intrinsic signal-to-noise ratio for a body-size birdcage coil loaded with different human subjects at 64 and 128 MHz. *Appl Magn Reson* 2005;29:5–18.
7. Quesson B, de Zwart JA, Moonen CTW. Magnetic resonance temperature imaging for guidance of thermotherapy. *J Magn Reson Imaging* 2000;12:525–533.
8. Shapiro EM, Borthakur A, Reddy R. MR imaging of RF heating using a paramagnetic doped agarose phantom. *MAGMA* 2000;10:114–121.
9. Shapiro EM, Borthakur A, Shapiro MJ, Reddy R, Leigh JS. Fast MRI of RF heating via phase difference mapping. *Magn Reson Med* 2002;47:492–498.
10. Cline H, Mallozzi R, Li Z, McKinnon G, Barber W. Radiofrequency power deposition utilizing thermal imaging. *Magn Reson Med* 2004;51:1129–1137.
11. Kowalski ME, Behnia B, Webb AG, Jin J-M. Optimization of electromagnetic phased-arrays for hyperthermia via magnetic resonance temperature estimation. *IEEE Trans Biomed Eng* 2002;49:1229–1241.
12. Armenean C, Perrin E, Armenean M, Beuf O, Pilleul F, Saint-Jalmes H. RF induced temperature elevation near metallic wires in clinical magnetic resonance imaging. *Magn Reson Med* 2004;52:1200–1206.
13. Alecci M, Collins CM, Smith MB, Jezzard P. Radio frequency magnetic field mapping of a 3 Tesla birdcage coil: experimental and theoretical dependence on sample properties. *Magn Reson Med* 2001;46:379–385.
14. Pennes HH. Analysis of tissue and arterial blood temperatures in the resting human forearm. *J Appl Physiol* 1948;1:93–122.
15. Collins CM, Li S, Smith MB. SAR and B_1 field distributions in a heterogeneous human head model within a birdcage coil. *Magn Reson Med* 1998;40:847–856.
16. Bernardi P, Cavagnaro M, Pisa S, Piuze E. Specific absorption rate and temperature elevation in a subject exposed in the far-field of radio-frequency sources operating in the 10-900MHz range. *IEEE T Biomed Eng* 2003;50:295–303.
17. Katscher U, Findelee C, Voigt T. Experimental estimation of local SAR in a multi-transmit system. In: 16th ISMRM, Honolulu, 2009. p 4512.